48th AIAA Aerospace Sciences Meeting Including the New Horizons Forum and Aerospace Exposition
4 - 7 January 2010, Orlando, Florida

AIAA 2010-108

Low-Frequency Unsteadiness in the DNS of a Compression Ramp Shockwave and Turbulent Boundary Layer Interaction

Stephan Priebe[*], M. Pino Martín[†]

The direct numerical simulation (DNS) of a compression ramp shockwave and turbulent boundary layer interaction (STBLI) is presented. The ramp angle is 24°, and the inflow boundary layer conditions are Mach 2.9 and $Re_\theta = 2900$. For the discretization of the inviscid fluxes, a modified weighted essentially nonoscillatory (WENO) scheme is used. The numerical code has previously been validated in the context of a compression ramp DNS against experiments at matching flow conditions.[1,2] The present DNS covers a time of $1000\delta/U_\infty$ $(350L_{sep}/U_\infty)$, making an analysis of the low-frequency unsteadiness that occurs in this kind of flow possible. The dominant scales in the flow are investigated by spectral analysis. The statistical link between the low-frequency shock motion and the upstream and downstream flow is investigated.

I. Introduction

The interaction of a shockwave with a turbulent boundary layer is ubiquitous in compressible flow applications. Examples of flows involving such interactions are the flows over deflected control surfaces or inside super- and hypersonic engine inlets. A key feature of STBLIs is their strong unsteadiness. When the flow is separated, the shock is seen to oscillate in the streamwise direction at relatively low frequency. If U_∞/δ is the characteristic frequency of the energetic scales in the inflow boundary layer (here, U_∞ is the freestream velocity and δ is the 99% thickness of the boundary layer), then the characteristic frequency of the shock motion will typically be 1 to 2 orders of magnitude lower, i.e. $O(0.1 - 0.01U_\infty/\delta)$.[3,4]

The cause of the low-frequency unsteadiness is still under debate. It has been proposed that the shock motion is due to the upstream boundary layer, see e.g. Ganapathisubramani, Clemens and Dolling,[5] or, alternatively, that it is due to the downstream separated flow, see e.g. Dupont et al.,[6] Dussauge et al.,[7] and Piponniau et al.[8]

Recent large eddy simulations (LESs) and direct numerical simulations (DNSs) capture the low-frequency unsteadiness. Touber and Sandham[9] performed the LES of a reflected STBLI at Mach 2.3 and Re_θ 5900, matching experimental flow conditions.[7] The low-frequency unsteadiness is present in their simulations at the same frequency as in experiments. They use a new inflow technique to ensure that no artificial low-frequency forcing is introduced into the computation. A stability analysis is also performed, and this shows the presence of a global instability mode which could be connected to the observed low-frequency unsteadiness. Wu and Martin[1,10] performed the DNS of a 24° compression ramp at Mach 2.9 and Re_θ 2300. They validated their results (in terms of separation length, mean wall-pressure distribution, evolution of the mean flow through the interaction) against experiments by Bookey et al.[11,12] at matching conditions. In addition, Ringuette, Wu and Martin[2] validated the fluctuating wall-pressure in the DNS against the experiments by Ringuette and Smits.[13] The shock motion was inferred in the DNS from wall-pressure fluctuations, and mass-flux fluctuations in the freestream, and its frequency was found to agree with a scaling previously proposed.[7] Priebe, Wu and Martin[14] performed the DNS of a reflected shock STBLI at Mach 2.9 and Re_θ 2300 with a flow deflection through the incident shock of 12°. Both the simulations by Wu and Martin,[1,10] and by Priebe, Wu and Martin[14] have relatively short signal lengths and cover only approximately 2-3 periods of the low-frequency unsteadiness (based on its dominant frequency).

---

[*] Graduate Student, Department of Mechanical and Aerospace Engineering, Princeton University. Visiting Graduate Student, Department of Aerospace Engineering, University of Maryland, College Park.

[†] Associate Professor, Department of Aerospace Engineering, University of Maryland, College Park.

In the present paper, we present the DNS of a compression ramp configuration, which covers a significantly longer time than our previous simulation.[1]

II. Flow Configuration and Computational Setup

The flow configuration considered in the present work is a 24° compression ramp, as shown schematically in figure 1. We perform the direct numerical simulation of the flow of a turbulent boundary layer over this compression ramp. The conditions of the inflow boundary layer are Mach 2.9 and $Re_\theta = U_\infty \theta / \nu_\infty = 2900$ (where U_∞ denotes the freestream velocity, ν_∞ the kinematic viscosity, and θ the momentum thickness). The Karman number is $\delta^+ = \delta u_\tau / \nu_w = 340$ (where u_τ denotes the friction velocity and ν_w the kinematic viscosity at the wall).

Figure 2 shows the computational domain for the DNS, which extends 7.9δ in the streamwise direction from the inflow plane to the corner and 6.4δ from the corner to the outflow plane (here, δ denotes the 99% thickness of the inflow boundary layer). In the spanwise direction, the computational domain measures 2.0δ, and in the wall-normal direction, it measures approximately 4.4δ at the inflow plane. As indicated in the figure, the boundary condition at the inflow plane is provided by an auxiliary simulation, which is a modified boundary layer DNS. The details of this auxiliary DNS, particularly the nature of the modification, will be described in detail in section III. The computational grid is clustered both in the wall normal direction (near the wall), and in the streamwise direction (near the corner to achieve adequate resolution in the interaction region). In the spanwise direction, the grid is uniform. A coarse version of the grid is shown in figure 3 in a streamwise-wall normal plane (x, z-plane). The actual grid contains a total of close to 20 million gridpoints ($1024 \times 160 \times 128$ grid points in the streamwise, spanwise and wall-normal directions, respectively.)

The numerical scheme used here is identical to that used and validated by Wu and Martin[1] in the DNS of a 24° compression ramp flow at Mach 2.9 and $Re_\theta = 2300$. We use a 4th-order accurate weighted essentially nonoscillatory scheme (WENO), which is both linearly and non-linearly optimized.[1,15,16] For the spatial discretization of the viscous fluxes, 4th-order accurate central differencing is used, and time-integration is performed with a 3rd-order accurate, low-storage Runge-Kutta algorithm.

The present DNS code was validated by Wu and Martin[1] (in terms of the separation length, mean-wall pressure distribution and velocity profiles through the interaction) against the experiments of Bookey, Wyckham and Smits[12] at matching flow conditions. In addition, the fluctuating wall pressure in Wu and Martin's DNS was validated by Ringuette, Wu and Martin[2] against the experiments of Ringuette and Smits.[13]

At the wall, a no-slip, isothermal boundary condition is used. The prescribed wall temperature is 307K, which is close to the adiabatic wall temperature. At the top and outlet boundaries, a supersonic exit boundary condition is used. A significant difference between the present simulation and that of Wu and Martin[1] is the type of inlet boundary condition used. Wu and Martin[1] use a rescaling box at the inlet of the computational domain. In contrast, in the present simulation, the inlet boundary condition is prescribed from a separate, auxiliary boundary layer DNS (described below). This means that the rescaling is not performed as part of the compression ramp DNS. Instead, it is performed as part of the auxiliary DNS, the results of which are then used as an inflow boundary condition for the compression ramp DNS. Performing a separate boundary layer DNS to generate the inflow boundary condition has several advantages, including the possibility of reusing the boundary condition for other STBLI simulations.

III. The Auxiliary DNS

Details of the auxiliary DNS may be found in Priebe and Martin.[17] We briefly summarize the results here.

The auxiliary simulation is a modified DNS of a Mach 2.9, $Re_\theta = 2900$ boundary layer. The modification consists in applying a 'flow filter' in the freestream. The rationale for using such a filter is as follows: In our experience, when the DNS is run for long times (of the order of several 100s of δ / U_∞), it becomes apparent that the rescaling[18] forces an acoustic mode in the freestream. The fluctuations are seen to grow in the freestream as the simulation progresses. The growth rate is relatively moderate, but over the long runtimes required here, the level of fluctuations in the freestream eventually becomes unacceptable. The increased turbulence level in the freestream is an unphysical artifact of the simulations, which we damp by filtering the conservative variables in the freestream, according to:

$$u(x,y,z) = \overline{u(z)} + f(z)u'(x,y,z) \tag{1}$$

where f is the filter function ($f = 0$ means that the flow is left unchanged and $f = 1$ means that the fluctuations are completely damped), u is the filtered variable, $\overline{u}$ is the streamwise-spanwise mean of the unfiltered variable, u' is the local fluctuation of the unfiltered variable.

The filter function that we use is plotted in figure 4. A key point to note from this figure is that the filter only acts in the freestream, above the region of intermittency. The filter is only 'switched on' above a wall-normal coordinate of z = 1.5δ in the freestream. The boundary layer flow itself is not subject to the filtering.

We have shown in[17] that the filtering successfully damps the acoustic mode in the freestream, while maintaining the accuracy of the simulation. To illustrate the damping of the fluctuations in the freestream, figure 6 compares the massflux signal in the freestream of the filtered DNS with its unfiltered counterpart. The van Driest-transformed velocity profile of the filtered DNS is shown in figure 5.

Figure 7 shows the streamwise velocity spectrum as a function of wavenumber in the middle of the log layer ($z^+ = 60$) of the filtered boundary layer DNS. As expected, a peak is visible at the rescaling wavenumber and at its higher harmonics. Most importantly, however, the filtering does not introduce any significant forcing in the spectrum. This was verified for all heights across the boundary layer. Figure 8 shows the streamwise velocity spectrum in the freestream, where the dominant energy is at the rescaling wavenumber and its higher harmonics. Again, the filtering does not introduce any forcing.

IV. General Description of the Flowfield

We now turn our attention away from the auxiliary DNS and back to the principal DNS of the compression ramp. The flow conditions are summarized in table 1. We note that these flow conditions are somewhat different from those in the previous DNS of Wu and Martin,[1] the experiments of Bookey, Wyckham and Smits,[12] and the experiments of Ringuette and Smits.[13] The Reynolds number in the present DNS is somewhat higher at $Re_\theta = 2900$, as compared to a value of 2300 in the previous DNS.

Figure 9 shows a typical instantaneous numerical Schlieren visualization for the present DNS. The flow is from left to right. The instantaneous organization of the flow in a streamwise-wall normal plane is apparent, including the large-scale bulges in the inflow boundary layer, the shock wave, and the strong gradients (large numerical Schlieren index) in the separated, downstream flow. A series of 'shocklets' can be seen in the flow downstream of the corner, between the boundary layer edge and the shockwave. These shocklets are typically associated with the turning of the flow near reattachment.

The three-dimensional instantaneous organization of the flow is apparent from figure 10, which shows an isosurface of the magnitude of density gradient ($|\nabla\rho| = 2.5\rho_\infty/\delta$), colored by the streamwise velocity component. The color map is chosen such that the color 'red' corresponds to the freestream velocity and 'blue' corresponds to reversed flow. It is apparent, then, that the flow at the corner is reversed. The large-scale bulges in the incoming boundary layer are also beautifully brought out in this visualization. Since the iso-surface is partially translucent, several shocklets can be seen in the flow near reattachment (located 'behind' the shock in this visualization).

Figure 11 shows the skin-friction and wall-pressure distribution along the streamwise direction. The abscissa in this plot is x^*, which is the distance along the wall, rather than the Cartesian coordinate, x. The skin friction and wall pressure shown here are averaged in time and across the spanwise direction, which is statistically homogeneous. Identifying the region of separated flow with the region of negative skin friction, the separation point is located at $x^* = -2.1\delta$, upstream of the corner. The reattachment point is located at $x^* = 0.9\delta$. The total separation length is thus $L_{sep} = 3.0\delta$.

The mean wall pressure distribution displays a 'plateau' as is indicative of separated flow.

	M	Re_θ	θ (mm)	δ^* (mm)	C_f	δ (mm)	ρ_∞ (kg/m^3)	U_∞ (m/s)	T_∞ (K)
present DNS	2.91	2900	0.47	2.58	0.00216	7.1	0.076	610.2	109.1

Table 1. Conditions for the incoming turbulent boundary layer.

V. Spectral Analysis of the Flowfield

In the present paper, we focus our analysis of the DNS dataset on the low-frequency unsteadiness of the shock system. We bring out the dominant scales in the flow through spectral analysis and investigate the statistical link between the shock motion and (a) the inflow boundary layer and (b) the separated flow.

The shock motion is apparent from wall-pressure signals. Figure 12 plots three signals, which were obtained at different streamwise locations from the DNS. The signals have been spanwise averaged. It is apparent that the pressure displays a markedly different behavior at the three locations shown. In the upstream, undisturbed boundary layer (signal shown in light gray), there are no low-frequency oscillations, whereas near the mean-flow separation point (signal shown in dark gray), low-frequency oscillations are clearly apparent (and seem to be the dominant contribution to the r.m.s. of the signal). Further downstream, at the corner (signal shown in black), the low-frequency oscillations still seem to be present although they are clearly not dominant.

The length of the time history shown in Figure 12 corresponds to the complete time history available from the DNS, which is equal to over $1000\delta/U_\infty$. When investigating the low-frequency unsteadiness, the appropriate length scale seems to be the length of the separated flow region,[7] L_{sep}, based on which the time duration of the DNS is approximately $350L_{sep}/U_\infty$.

Figure 13 shows the power spectral densities of different wall-pressure signals. The power spectra are pre-multiplied and normalized by the rms of the signals (i.e. the area under each curve is equal to unity).

Figure 13(a) plots the power spectrum in the undisturbed boundary layer. The bulk of the energy is contained in a broadband peak associated with the turbulent motions. The peak is centered at a frequency of approximately U_∞/δ, as expected. Superimposed on the broadband peak are narrow peaks associated with the rescaling frequency and its higher harmonics (the second and third harmonic are visible). These peaks have compact support in frequency, and they contain little energy compared to the turbulence. Furthermore, they are at least a decade away from the low-frequency range associated with the shock motion and hence do not pollute the range of frequencies that are of interest here. We note that there is no energy at the low frequencies associated with the shock motion, that is, around values of $St = fL_{sep}/U_\infty$ of the order of 0.01.

Figure 13(b) plots the power spectrum near the mean-flow separation point. The broadband turbulence peak and the narrowband rescaling peaks are present, but more than 50% of the energy is contained at much lower frequencies associated with the shock motion. The range of frequencies found here agrees with that determined by Dussauge et al.[7] They perform a survey of STBLI experiments and find that, across a range of flow conditions and configurations, the frequency of the shock motion lies in the range $St = 0.02 - 0.05$.

Figure 13(c) shows the power spectrum near the mean-flow reattachment point. Some energy is still present in the range of frequencies associated with the shock motion, but the bulk of the energy has shifted back to the turbulent scales. In the downstream flow (see figure 13(d)), the energy at the low frequencies is further reduced, and almost all of the energy is contained in the broadband peak associated with the turbulence in the downstream flow.

A different way of presenting the power spectra is given in figure 14, where contours of power spectral density are shown as a function of streamwise distance along the wall, x^*, and of non-dimensional frequency. The contour map is saturated at a level of $PSD = 0.6$ for greater clarity. In the undisturbed boundary layer, the bulk of the energy is contained in the turbulent motions. Near the mean-flow separation point, most of the energy is contained at much lower frequencies associated with the shock motion. In the downstream flow, the bulk of the energy is contained again in the turbulent scales.

The above distribution of scales is in agreement with the experiments of Dupont, Haddad and Debiève[6] for a low-Reynolds number reflected shock boundary layer interaction.

So far, we have only considered signals obtained at the wall. We now move away from the wall and investigate signals inside the flow. First, let us look at the shock motion in the freestream. We determine the mean shock location using a pressure-threshold criterion. At fixed height above the wall, the location of the shock is identified with the first point encountered in a streamwise sweep of the computational domain (starting from the inlet), for which the pressure is greater than $1.27p_\infty$. Figure 15 plots the power spectrum of the pressure obtained at the mean shock location at $z = 1.4\delta$. Since the shock moves across this point, the bulk of the energy is contained in a broadband peak in the range of low frequencies associated with the shock motion.

Figure 16 shows massflux spectra obtained in the downstream and separated flow region. Figure 16(a) shows the spectrum of streamwise massflux, obtained at a location inside the reversed flow region above the corner. Interestingly, the spectrum is quite ‘flat’. It consists of a broadband peak spanning the entire range of investigated frequencies. This indicates that the motions inside the separation bubble have a large range of scales. We note that there is a significant amount of energy at the low frequencies characteristic of the shock motion.

Figure 16(b) shows the spectrum of streamwise massflux, obtained at the location of maximum rms in the massflux above the corner. This point most likely lies in the separated shear layer, which lies above the separation bubble. The spectrum displays a broadband peak, which is centered around a frequency significantly lower than the characteristic turbulence frequency in the incoming boundary layer. This indicates that the characteristic frequency of the turbulent motions in the shear layer is lower than that of the energetic eddies in the incoming boundary layer. Furthermore, the spectra carry significant energy in the low frequency range of the shock motion.

VI. Statistical Link between Shock Motion and Upstream and Downstream Flow

The physical mechanism that drives the low-frequency shock unsteadiness is still under debate. It has been proposed that an upstream mechanism is at work, whereby the shock motion is driven by a low-frequency mechanism in the upstream boundary layer. Evidence for such an upstream mechanism is given by, e.g., Ganapathisubramani, Clemens and Dolling.[5] In contrast to this upstream-driven mechanism, it has also been proposed that the shock motion is driven by the downstream, separated flow, evidence for which is given by, e.g., Dupont et al.,[6] Dussauge et al.,[7] and Piponniau et al.[8]

In this section, we investigate the statistical link between the shock motion and the upstream and downstream flow from the DNS dataset. In order to investigate the statistical link, we consider the magnitude-squared coherence function (MSC). The MSC between two signals a and b is defined as

$$coh(f) = \frac{|P_{ab}(f)|^2}{P_{aa}(f)P_{bb}(f)} \tag{2}$$

where P_{aa} and P_{bb} are the power spectral densities of the signals a and b, respectively, and P_{ab} is the cross-power spectral density. The coherence function indicates, as a function of frequency, how well signal a corresponds to signal b. The MSC function takes values that range from 0 to 1, where a value of 0 indicates that the two signals are unrelated, and a value of 1 indicates that a linear relationship between the two signals exists.

VI.A. Statistical Link between Shock Motion and Downstream Flow

As an indicator for the shock motion, we use the pressure at the mean-shock location in the freestream (at $z = 1.4\delta$). The spectrum for this signal was shown in figure 15. The MSC between the ‘shock-indicator signal’ and several wall-pressure signals in the separated flow is shown in figure 17. As expected, all plots show a significant coherence at the rescaling frequency and at its second and third harmonic. This behavior is spurious and unphysical, but we argue that it is acceptable for investigating the low-frequency shock unsteadiness, since the rescaling frequency lies a decade above the dominant frequencies associated with the shock motion and hence does not pollute the low-frequency part of the spectra or coherence plots that is of interest here.

Figure 17(a) shows the MSC between the shock-indicator signal (signal a) and the wall pressure near the mean-flow separation point (signal b). There is no significant coherence at high frequencies (except for the rescaling frequency and its higher harmonics, as discussed above). In the low frequency range of the shock motion, however, there exists a strong coherence between the two signals. The value of the MSC is almost 1 in this range indicating a near-linear relationship between the two signals. We thus conclude that the shock motion in the freestream and the wall-pressure fluctuations near the separation point are related almost linearly, which is consistent with the experimental findings of Dupont et al.[6] for a reflected shock interaction.

In figures 17(b), 17(c) and 17(d), the location of signal a (the shock-indicator signal in the freestream) is kept fixed, while the location of signal b (the wall-pressure signal) is moved further downstream from one figure to the next. In figure 17(b), signal b is taken under the separated flow region at a point downstream of the shock motion region but still upstream of the corner; in figure 17(c), signal b is taken near the mean-flow reattachment point; and in figure 17(d), it is taken in the downstream flow. All plots show strong coherence in the range of low frequencies associated with the shock motion, indicating that the wall-pressure under the separation bubble, and slightly downstream of reattachment, undergoes low-frequency oscillations that are coherent with the shock motion in the freestream.

VI.B. Statistical Link between Shock Motion and Upstream Flow

Figure 18 shows the statistical link between the shock motion in the freestream and the upstream boundary layer. Signal a is taken to be the pressure at the mean-shock location at $z = 1.4\delta$, i.e. the same shock-indicator signal that was used in figure 17 above. Signal b is taken to be the wall-pressure under the undisturbed boundary layer in figure 18(a), and in figure 18(b) it is taken to be the massflux in the middle of the log layer ($z^+ = 60$).

In order to be able to draw statistical inferences from these plots, we have derived a 99.9% confidence limit, which is shown in the figures. If an estimate of the coherence lies above this line, then the probability that the two signals are, in fact, independent (i.e. that the *true* coherence is zero) is only 0.1%. In other words, if an estimate lies above the confidence limit shown, then the probability that the two signals have a true coherence that is greater than zero is 99.9%. The confidence limit has been determined from Monte Carlo simulations.

Both plots in figure 18 show a weak, but statistically significant coherence between the shock motion and the upstream flow in the DNS, in the sense that the coherence estimates lie above the 99.9% confidence limit, at least for some frequencies in the range of low frequencies associated with the shock motion.

VII. Conclusions

The direct numerical simulation of a compression ramp shockwave and turbulent boundary layer interaction is presented. The ramp angle is 24° and the inflow boundary layer is at Mach 2.9 and Re_θ 2900. The simulation covers a time of more than $1000\delta/U_\infty$, or approximately $350L_{sep}/U_\infty$.

The low-frequency unsteadiness in the DNS is apparent from wall-pressure signals near separation, as well as from signals at the mean shock location in the freestream. The time scales in the downstream and separated flows are determined. We investigate the statistical link between the shock motion (as indicated by a pressure signal in the freestream) and various signals in the upstream and downstream flow. Strong coherence, at the low frequencies of the shock motion, is observed with the downstream, separated flow. These findings are consistent with the experiments of Dupont et al.[6] for a reflected shock interaction. The coherence with the upstream, undisturbed boundary layer is shown to be statistically significant, but weak.

Acknowledgments

This work is supported by the Air Force Office of Scientific Research under grant AF/9550-09-1-0464.

References

[1] Wu, M. and Martin, M. P., "Direct Numerical Simulation of Supersonic Turbulent Boundary Layer over a Compression Ramp," *AIAA Journal*, Vol. 45, No. 4, 2007, pp. 879–889.

[2] Ringuette, M. J., Wu, M., and Martin, M. P., "Low Reynolds Number Effects in a Mach 3 Shock Turbulent Boundary Layer Interaction," *AIAA Journal*, Vol. 46, No. 7, 2008.

[3] Smits, A. J. and Dussauge, J. P., *Turbulent Shear Layers in Supersonic Flow*, Springer Verlag, New York, 2nd ed., 2006.

[4] Dolling, D., "Fifty Years of Shock-Wave/Boundary-Layer Interaction Research: What Next?" *AIAA Journal*, Vol. 39, No. 8, 2001, pp. 1517–1531.

[5] Ganapathisubramani, B., Clemens, N. T., and Dolling, D. S., "Effects of upstream boundary layer on the unsteadiness of shock-induced separation," *Journal of Fluid Mechanics*, Vol. 585, 2007, pp. 369–394.

[6] Dupont, P., Haddad, C., and Debiève, J. F., "Space and time organization in a shock-induced separated boundary layer," *Journal of Fluid Mechanics*, Vol. 559, 2006, pp. 255–277.

[7] Dussauge, J. P., Dupont, P., and Debiève, J. F., "Unsteadiness in Shock Wave Boundary Layer Interactions with Separation," *Aerospace Science and Technology*, Vol. 10, No. 2, 2006.

[8] Piponniau, S., Dussauge, J., Debiève, J., and Dupont, P., "A simple model for low-frequency unsteadiness in shock-induced separation," *Journal of Fluid Mechanics*, Vol. 629, 2009, pp. 87–108.

[9] Touber, E. and Sandham, N., "Large-eddy simulation of low-frequency unsteadiness in a turbulent shock-induced separation bubble," *Theoretical and Computational Fluid Dynamics*, Vol. 23, 2009, pp. 79–107.

[10] Wu, M. and Martin, M. P., "Analysis of Shock Motion in Shockwave and Turbulent Boundary Layer Interaction using Direct Numerical Simulation Data," *Journal of Fluid Mechanics*, Vol. 594, 2008, pp. 71–83.

[11] Bookey, P. B., Wyckham, C., Smits, A. J., and Martin, M. P., "New Experimental Data of STBLI at DNS/LES Accessible Reynolds Numbers," *AIAA Paper No. 2005-309*, Jan. 2005.

[12] Bookey, P. B., Wyckham, C., and Smits, A. J., "Experimental Investigations of Mach 3 Shock-Wave Turbulent Boundary Layer Interactions," *AIAA Paper No. 2005-4899*, June 2005.

[13] Ringuette, M. J. and Smits, A. J., "Wall-Pressure Measurements in a Mach 3 Shock-Wave and Turbulent Boundary Layer Interaction at a DNS-Accessible Reynolds Number," *AIAA Paper No. 2007-4113*, June 2007.

[14] Priebe, S., Wu, M., and Martin, M. P., "Direct Numerical Simulation of a Reflected-Shock-Wave/Turbulent-Boundary Layer Interaction," *AIAA Journal*, Vol. 47, No. 5, 2009, pp. 1173–1185.

[15] Martin, M. P., Taylor, E. M., Wu, M., and Weirs, V. G., "A Bandwidth-Optimized WENO Scheme for the Direct Numerical Simulation of Compressible Turbulence," *Journal of Computational Physics*, Vol. 220, 2006, pp. 270–289.

[16] Taylor, E. M., Wu, M., and Martin, M. P., "Optimization of Nonlinear Error Sources for Weighted Essentially Non-oscillatory Methods in Direct Numerical Simulations of Compressible Turbulence," *Journal of Computational Physics*, Vol. 223, 2006, pp. 384–397.

[17] Priebe, S. and Martin, M. P., "Analysis of the Low-Frequency Unsteadiness in the Direct Numerical Simulation of a Shockwave and Turbulent Boundary Layer Interactions," *AIAA Paper No. 2009-3711*, Jun. 2009.

[18] Xu, S. and Martin, M. P., "Assessment of Inflow Boundary Conditions for Compressible Boundary Layers," *Physics of Fluids*, Vol. 16, No. 7, 2004, pp. 2623–2639.

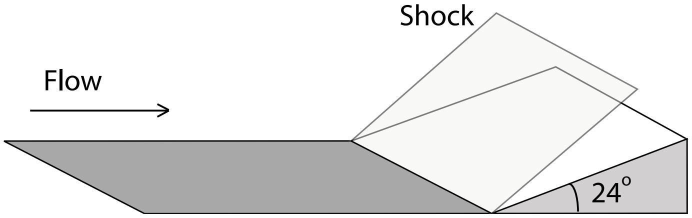

Figure 1. Schematic of flow over a compression ramp (inviscid case).

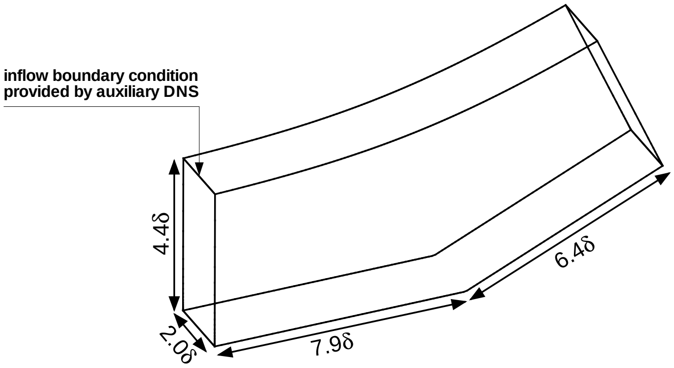

Figure 2. Computational domain for the DNS.

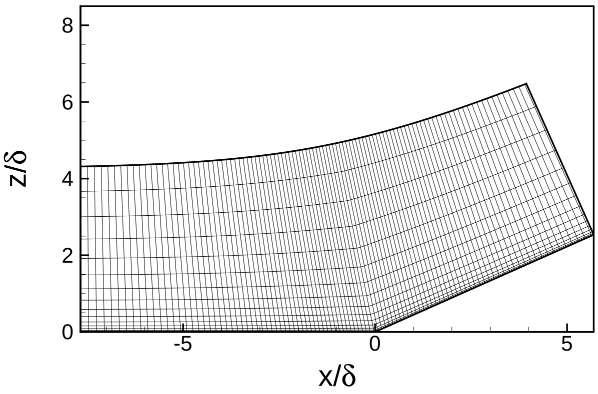

Figure 3. Sample grid for the DNS.

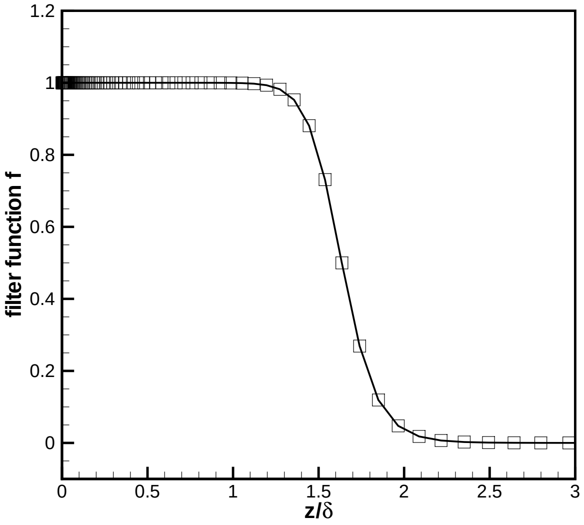

Figure 4. Filter function for the auxiliary DNS.

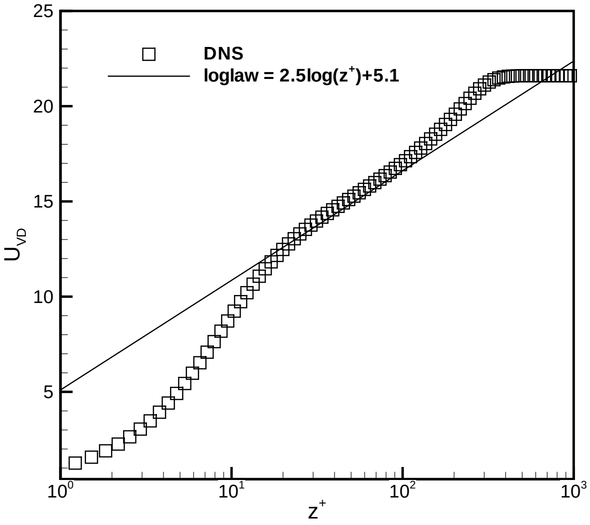

Figure 5. Van Driest-transformed velocity profile for the auxiliary DNS.

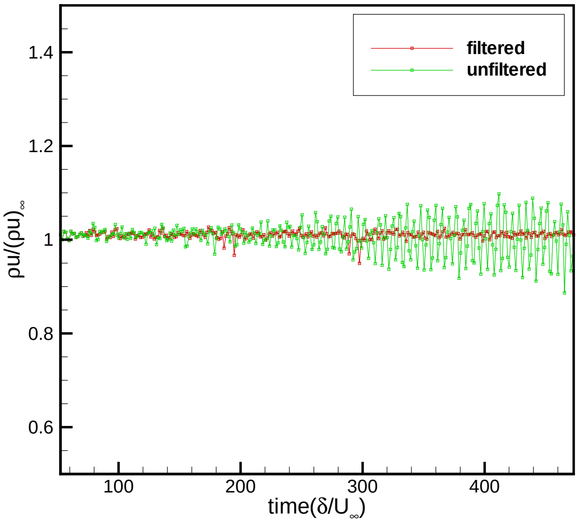

Figure 6. Spanwise-averaged mass-flux signal in the freestream ($z = 1.6\delta$) for the auxiliary DNS.

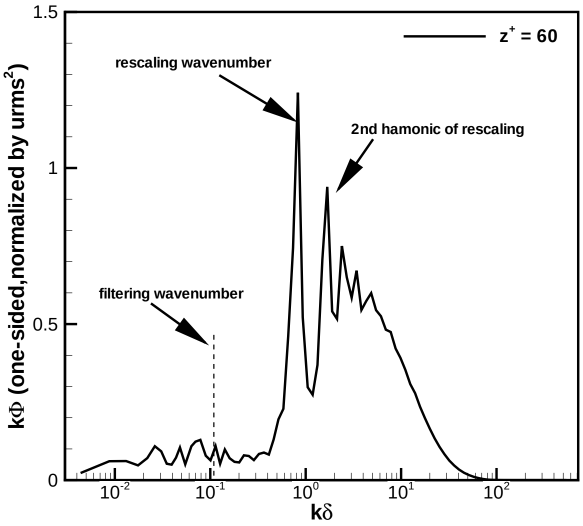

Figure 7. Streamwise velocity spectrum at $z^+ = 60$ (middle of log layer) for the auxiliary DNS.

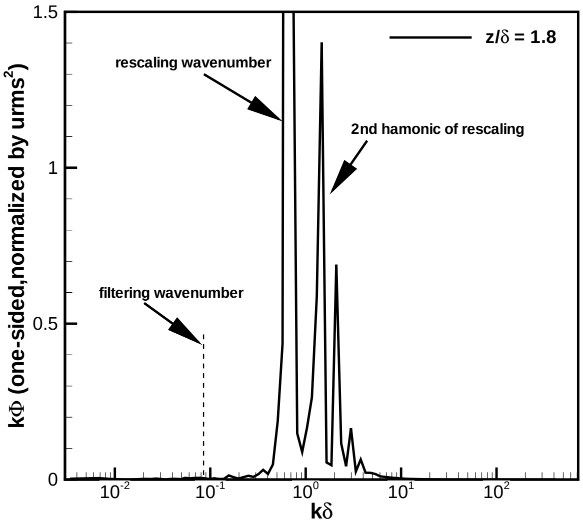

Figure 8. Streamwise velocity spectrum at $z = 1.8\delta$ for the auxiliary DNS.

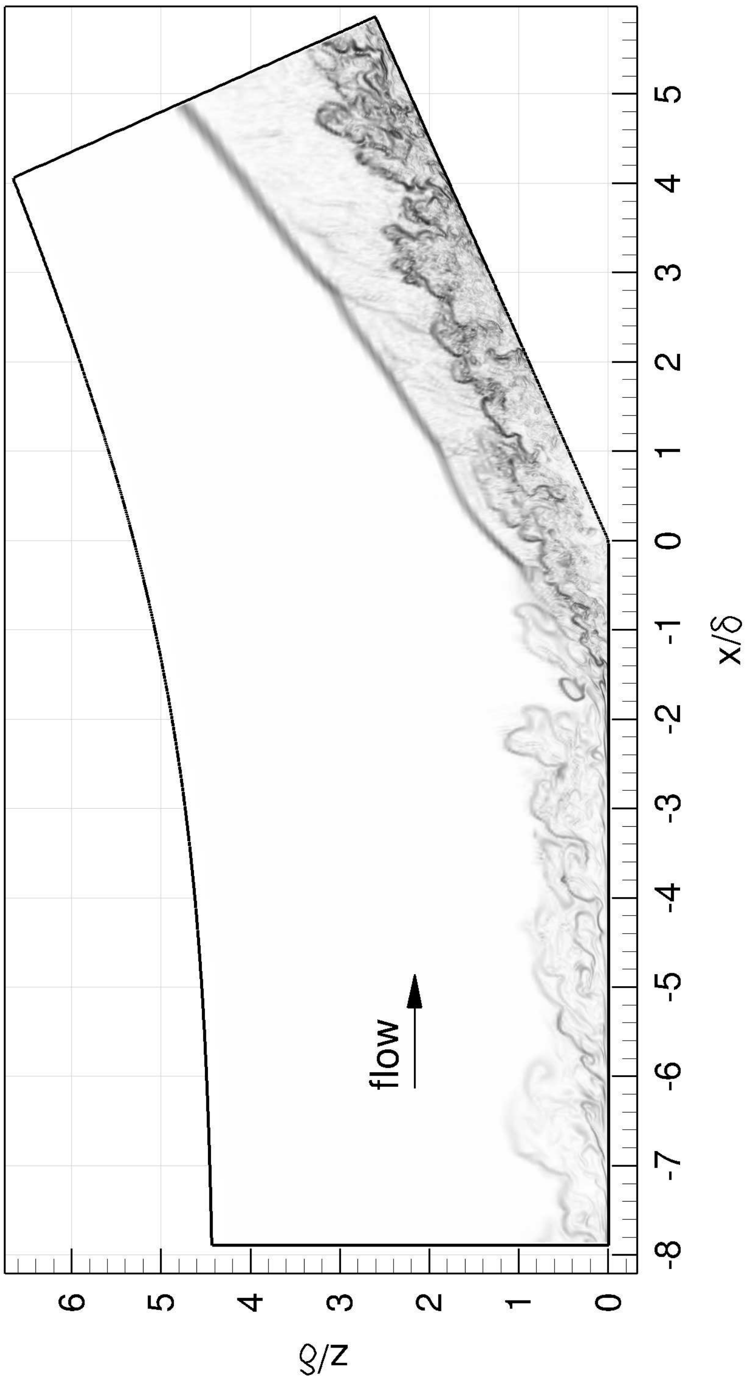

Figure 9. Typical instantaneous numerical Schlieren visualization of a streamwise-wall normal plane.

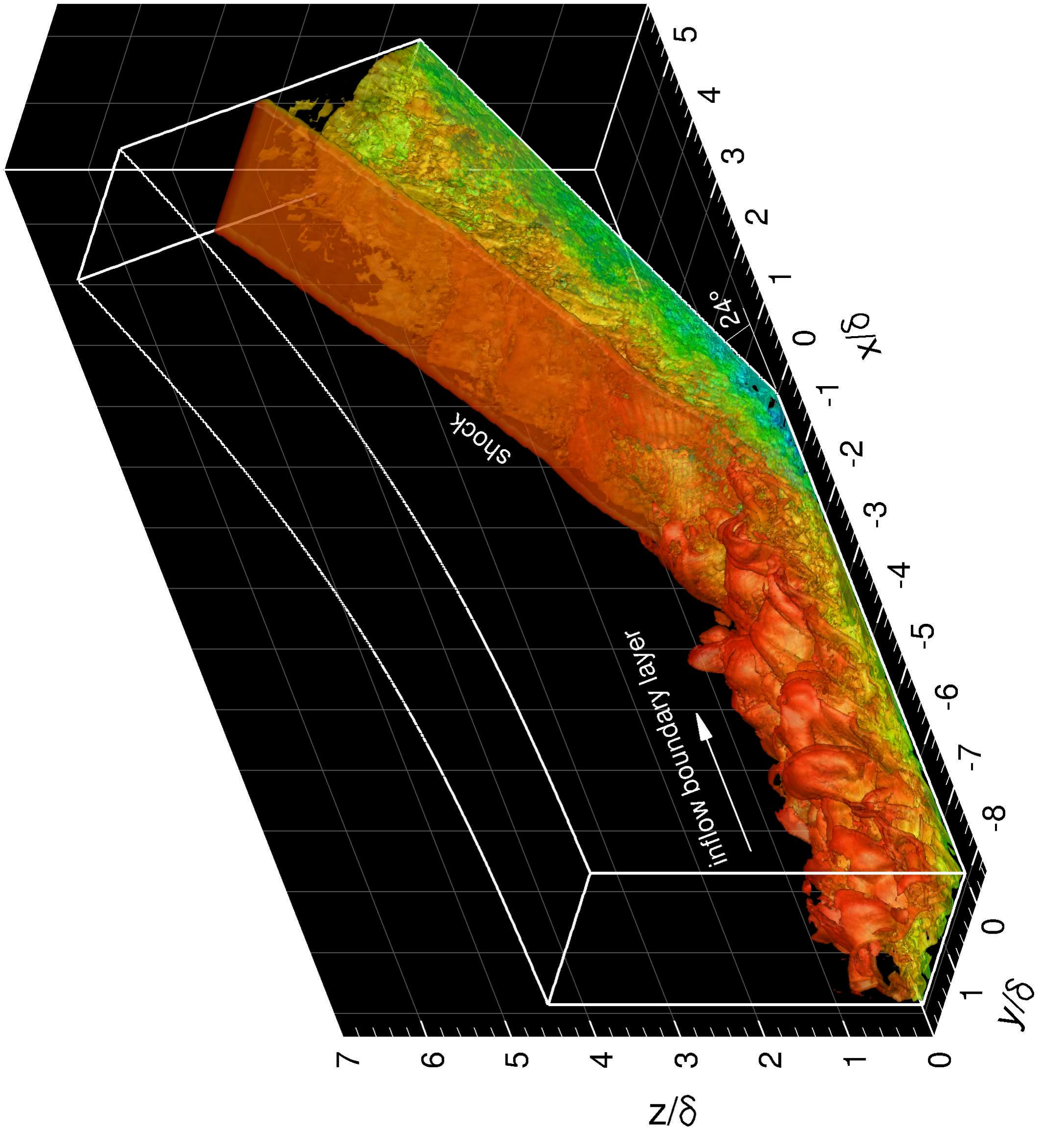

Figure 10. Instantaneous flow visualization. Isosurface of magnitude of density gradient ($|\nabla\rho| = 2.5\rho_\infty/\delta$), colored by the streamwise velocity component (where the color red corresponds to the freestream velocity, and blue corresponds to reversed flow).

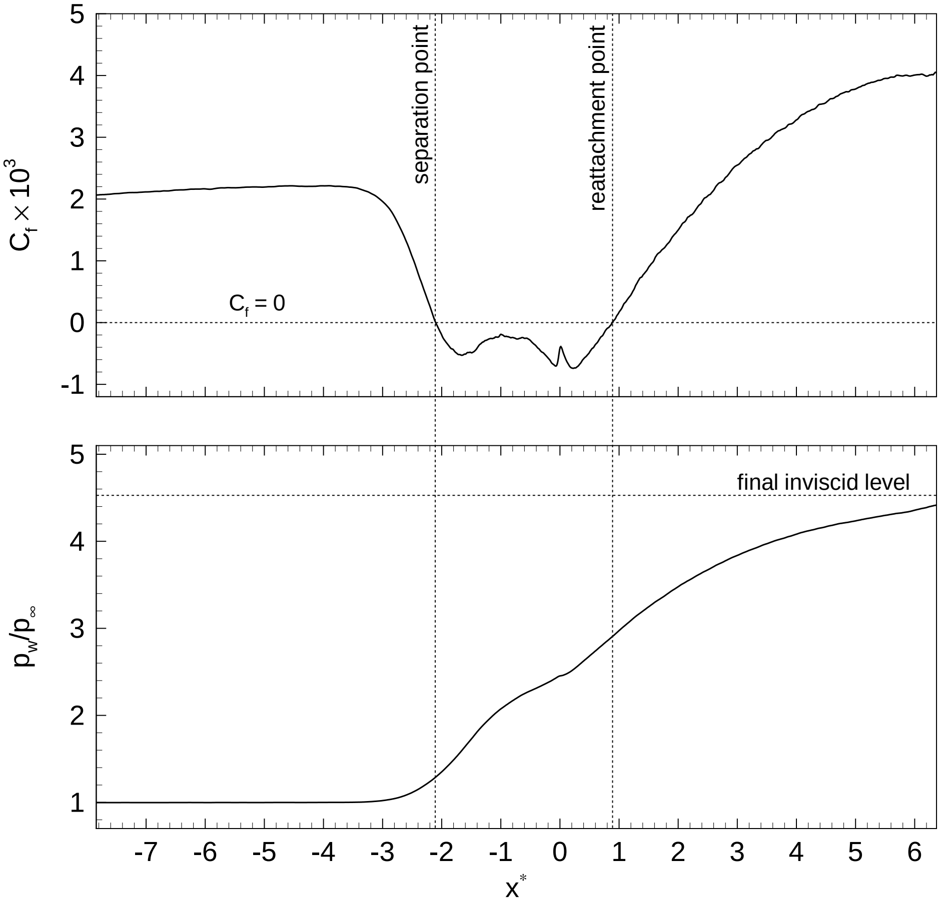

Figure 11. Mean distributions of C_f (top) and wall pressure (bottom).

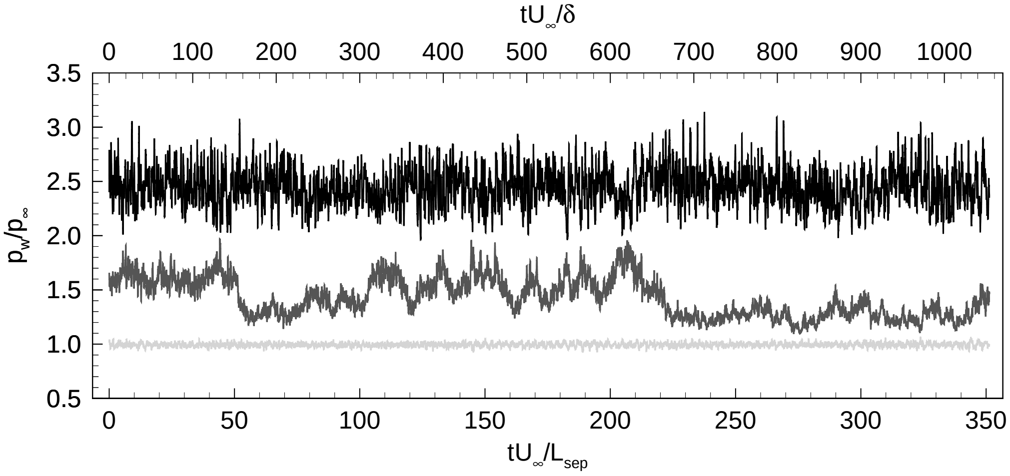

Figure 12. Wall-pressure signals at different streamwise locations (the light gray signal is obtained in the upstream flow, the dark gray signal near the mean-flow separation point, and the black signal at the corner.)

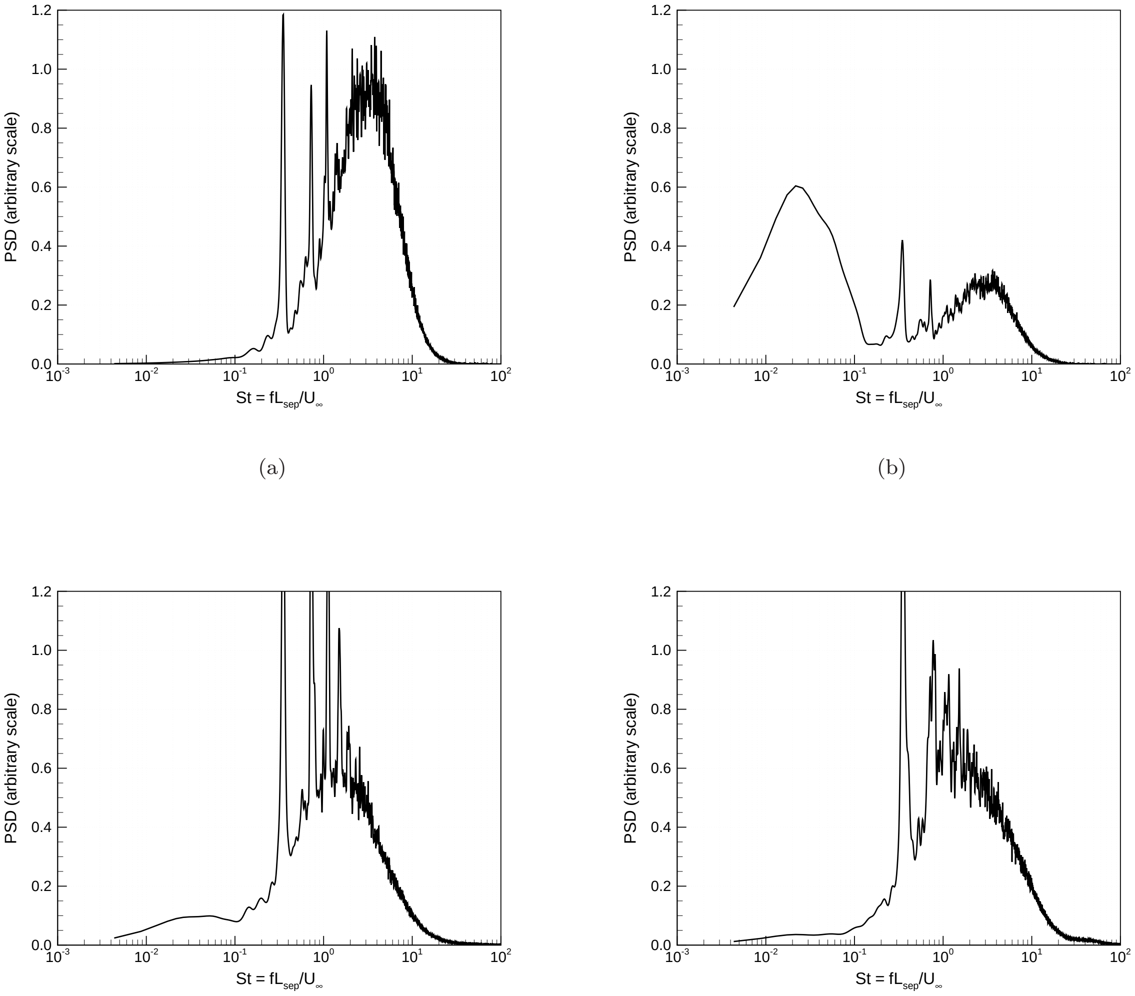

(a)

(b)

(c)

(d)

Figure 13. Pre-multiplied and normalized power spectra of wall pressure at different streamwise locations. (a) in the undisturbed boundary layer, (b) near the mean-flow separation point, (c) near the mean-flow reattachment point, and (d) in the downstream flow.

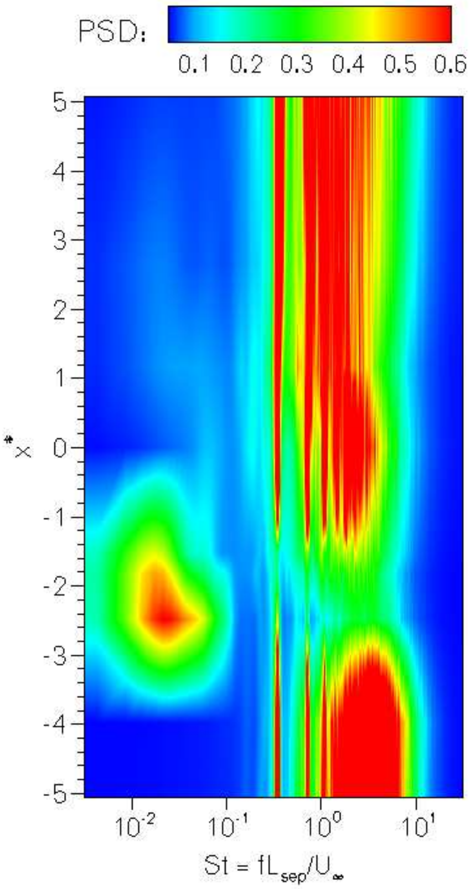

Figure 14. Contour map of premultiplied power spectrum. The variable x^* is the streamwise distance from the corner, measured along the wall.

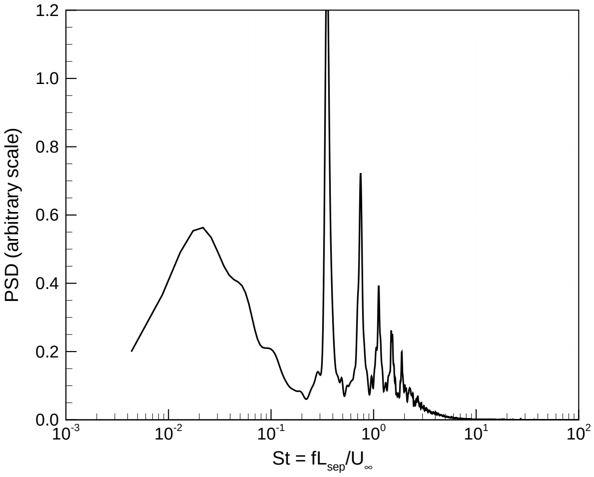

Figure 15. Pre-multiplied spectrum of pressure at mean shock location in the freestream ($z = 1.4\delta$).

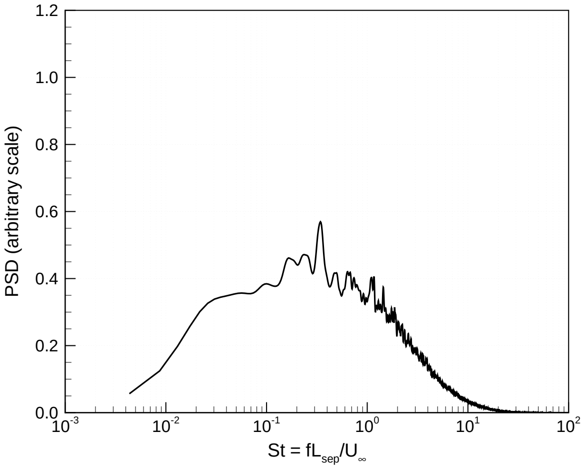

(a)

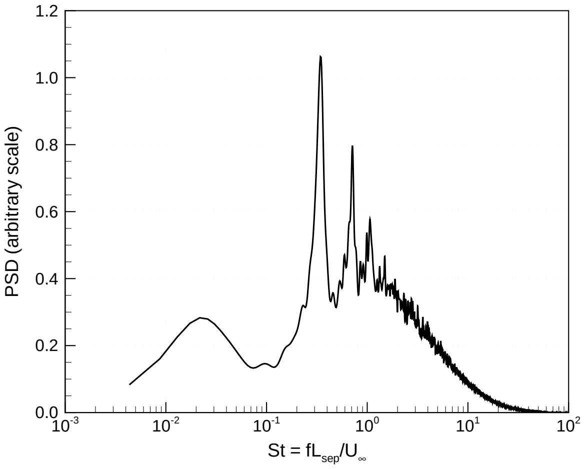

(b)

Figure 16. Pre-multiplied spectra of streamwise massflux in (a) the reversed flow region above the corner and (b) the shear layer above the separation bubble.

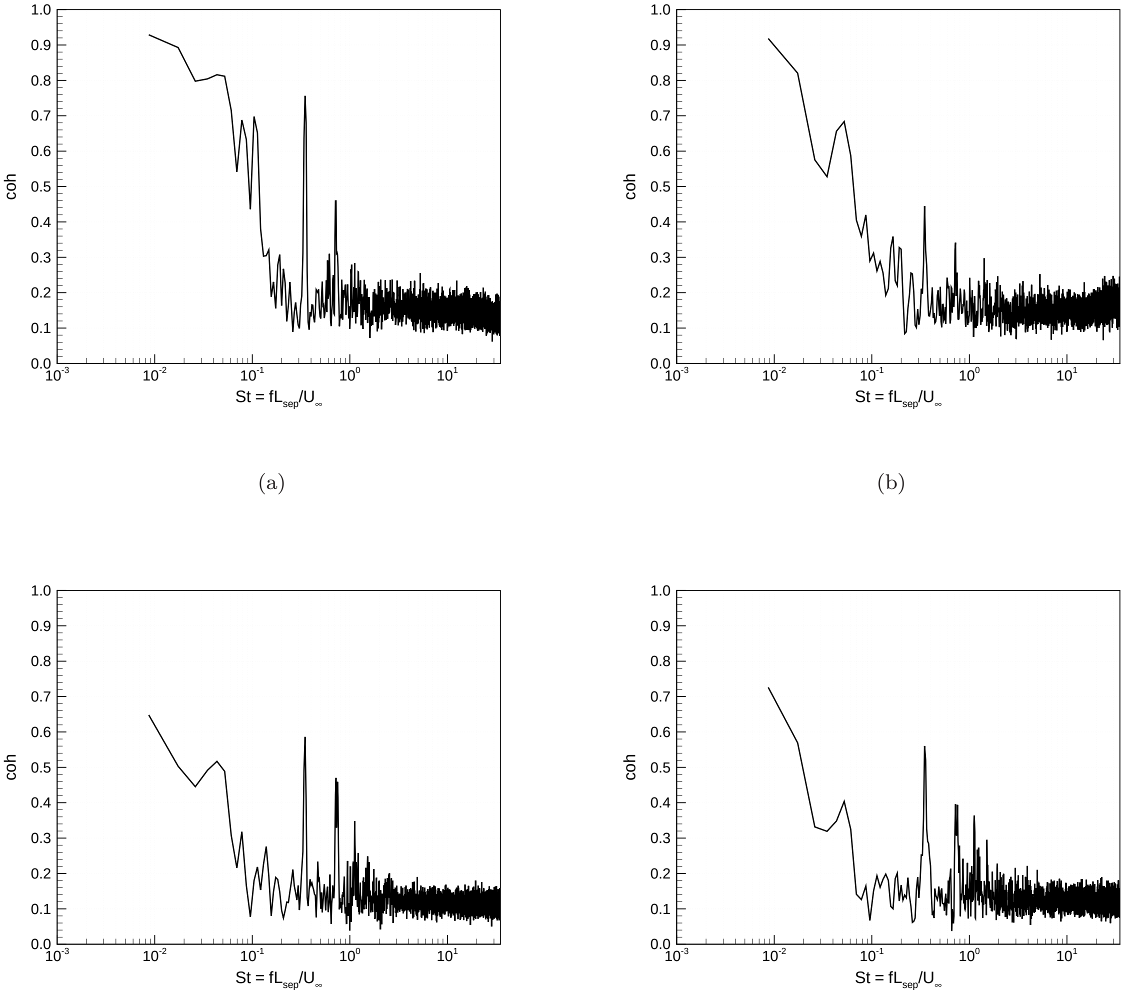

(a)

(b)

(c)

(d)

Figure 17. Statistical link between the shock motion and the separated flow. MSC between the pressure at the mean shock location in the freestream ($z = 1.4\delta$) and the wall pressure at different streamwise locations: (a) near the mean-flow separation point, (b) in the separated flow region upstream of the corner, (c) near the mean-flow reattachment point, and (d) in the downstream flow.

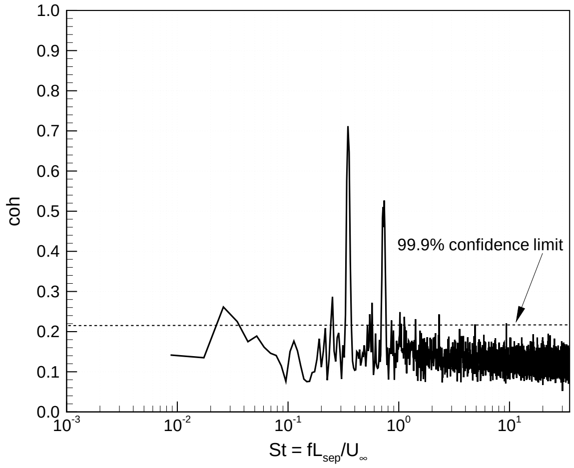

(a)

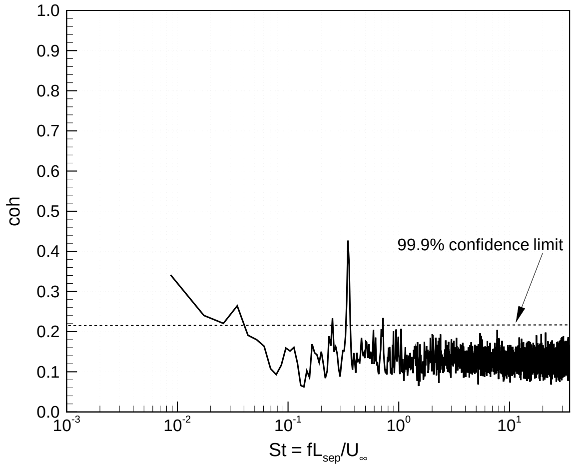

(b)

Figure 18. Statistical link between the shock motion and the upstream flow. MSC between the pressure at the mean shock location in the freestream ($z = 1.4\delta$) and (a) the upstream wall pressure, and (b) the massflux in the middle of the log layer ($z^+ = 60$) in the upstream boundary layer. See text for a derivation and explanation of the confidence limit shown in the figures.